



# Pd-doped or Pd impregnated 30% $\text{La}_{0.7}\text{Sr}_{0.3}\text{CoO}_3/\text{Al}_2\text{O}_3$ catalysts for $\text{NO}_x$ storage and reduction

Jon A. Onrubia-Calvo<sup>a</sup>, Beñat Pereda-Ayo<sup>a</sup>, Alejandro Bermejo-López<sup>a</sup>, Angel Caravaca<sup>b</sup>, Philippe Vernoux<sup>b</sup>, Juan R. González-Velasco<sup>a,\*</sup>

<sup>a</sup> Departamento de Ingeniería Química, Facultad de Ciencia y Tecnología, Universidad del País Vasco, UPV/EHU, Campus de Leioa, P. O. Box 644, ES-48080 Bilbao, Bizkaia, Spain

<sup>b</sup> Université de Lyon, Institut de Recherches sur la Catalyse et l'Environnement de Lyon, UMR 5256, CNRS, Université Claude Bernard Lyon 1, 2 Avenue A. Einstein, F-69626 Villeurbanne, France

## ARTICLE INFO

### Keywords:

Pd-doped  
Pd-impregnated  
Alumina-supported  
Perovskite  
 $\text{NO}_x$  storage and reduction

## ABSTRACT

Here we report the effects of the incorporation of palladium into 30%  $\text{La}_{0.7}\text{Sr}_{0.3}\text{CoO}_3/\text{Al}_2\text{O}_3$  catalyst by different methods on the  $\text{NO}_x$  storage and reduction behaviour. Several catalysts were prepared incorporating four palladium nominal loadings (0.75, 1.5, 2.25 and 3.0%) by doping the perovskite formulation (30%  $\text{La}_{0.7}\text{Sr}_{0.3}\text{Co}_{1-y}\text{Pd}_y\text{O}_3/\text{Al}_2\text{O}_3$ ) or by wetness impregnation over alumina-supported perovskite (y% Pd-30%  $\text{La}_{0.7}\text{Sr}_{0.3}\text{CoO}_3/\text{Al}_2\text{O}_3$ ). The results of X-Ray diffraction,  $\text{N}_2$  adsorption-desorption at  $-196^\circ\text{C}$ , electron microscopy, temperature programmed techniques, Raman and X-ray photoelectron spectroscopies demonstrated that the wetness impregnation method induces the formation of small PdO particles homogeneously distributed over the surface in strong interaction with the perovskite. Meanwhile, doping method leads to the formation of a mix between intraframework palladium species and surface agglomerated  $\text{PdO}_x$  particles with weaker interaction with the perovskite phase. Therefore, palladium accessibility and the synergetic effects with the perovskite are lower for Pd-doped samples. The NO-to- $\text{NO}_2$  conversion is similar irrespective of the palladium content and the incorporation method. This confirms the perovskite phase as the main active site for NO oxidation. However,  $\text{NO}_x$  adsorption during lean conditions and  $\text{NO}_x$  reduction to  $\text{N}_2$  during rich periods are significantly promoted after the incorporation of palladium, especially by impregnation method. This enhancement is assigned to better  $\text{NO}_x$  adsorption sites regeneration and to a promotion of  $\text{NO}_x$  reduction rate, respectively. Thus, the best De- $\text{NO}_x$  performance of Pd-impregnated catalysts is derived from the higher efficient use of the palladium active sites. Among the developed formulations, the 1.5% Pd-30% LSCO/ $\text{Al}_2\text{O}_3$  sample shows the best balance between  $\text{NO}_x$  removal efficiency and minimum palladium content. This sample shows a NO removal efficiency and nitrogen yield as high as 86.2% and 69.5%, respectively. Based on these results, the developed formulation is revealed as a promising alternative to the NSR model catalyst (1.5% Pt-15% BaO/ $\text{Al}_2\text{O}_3$ ) for  $\text{NO}_x$  removal in the automotive application.

## 1. Introduction

Diesel and lean burn engines operate under net oxidizing environment. These conditions lead to better fuel efficiency and lower  $\text{CO}_2$  emissions than stoichiometric gasoline engines. However, the operation with high air-to-fuel ratio makes three-way-catalyst (TWC) not efficient enough to meet EURO 6 standards regarding  $\text{NO}_x$  emissions. On account of this, lean-burn combustion engines require the implementation of different after-treatment systems.  $\text{NO}_x$  Storage and Reduction (NSR) and Selective Catalytic Reduction (SCR) technologies have been proposed as the most promising alternatives to overcome this problem [1].

NSR system operates under cyclic oxidizing-reducing conditions using 1.5% Pt-15% BaO/ $\text{Al}_2\text{O}_3$  as the model catalyst [2]. During the lean period (oxidizing conditions), Pt oxidizes NO to  $\text{NO}_2$ , which is adsorbed on Ba in the form of nitrates/nitrites. In the subsequent short rich period triggered by a post-injection of fuel,  $\text{NO}_x$  ad-species are released and reduced (preferentially) to  $\text{N}_2$  on Pt by a reductant such as  $\text{H}_2$ , CO or HC. Regarding SCR systems, they are based on the selectively catalyzed reaction of  $\text{NO}_x$  with externally added  $\text{NH}_3$  (produced by hydrolysis of urea) in an oxygen rich environment over Cu/zeolite-based catalysts [3]. The present work will focus on the NSR technology.

One of the main drawbacks of the state-of-the-art NSR catalysts is

\* Corresponding author.

E-mail address: [juanra.gonzalezvelasco@ehu.eus](mailto:juanra.gonzalezvelasco@ehu.eus) (J.R. González-Velasco).

<https://doi.org/10.1016/j.apcatb.2019.118052>

Received 6 May 2019; Received in revised form 29 July 2019; Accepted 3 August 2019

Available online 05 August 2019

0926-3373/ © 2019 Elsevier B.V. All rights reserved.

the high cost and the poor thermal stability of the Pt active phase [4]. In this sense, La-based perovskites have attracted attention over the past 30–40 years as a potential alternative to noble metals in oxidation processes [5]. The perovskite lattice can be described using the general formula  $ABO_3$ . The catalytic activity of perovskites can be easily tuned by substituting a small fraction of A or B-sites atoms with other cations. This allows designing efficient perovskite formulations as alternative to Pt-based catalysts for the NSR process, since NO-to- $NO_2$  oxidation is considered as a critical primary step in the NSR technology [6].

We recently reported that  $La_{0.7}Sr_{0.3}CoO_3$  perovskite improved significantly NO oxidation activity beyond that of the model Pt-based catalyst formulation [7]. The developed formulation also exhibits high  $NO_x$  adsorption during lean conditions. However, one of the primary limitations of the bulk  $La_{0.7}Sr_{0.3}CoO_3$  is the low exposed surface area derived from the high calcination temperature required for the crystallization of the perovskite. The impregnation of 30% of  $La_{0.7}Sr_{0.3}CoO_3$  perovskite over  $\gamma-Al_2O_3$  has been reported as a promising alternative to overcome this limitation [8]. The higher  $NO_x$  removal efficiency of alumina-supported perovskite samples was mainly ascribed to the easier diffusion of intermediate compounds from oxidation sites to the adsorption sites.

However, the  $NO_x$  reduction capacity of the perovskite-based catalysts is still lower than that of the model Pt-based catalyst [8]. The incorporation of small amounts of noble metals has been widely accepted as an alternative to enhance the  $NO_x$  abatement [9–11]. Among them, palladium has shown higher thermal stability than Pt-based formulations [12]. Some reports have described the incorporation of small amounts of Pd in the bulk perovskite formulation as a way to enhance the  $NO_x$  reduction capacity, especially in TWC systems [13–16]. Two approaches can be used for the incorporation of Pd in perovskite-based formulations: via impregnation [17], and/or by doping the perovskite formulation [16,20,21]. The insertion of the Pd within the B site of the perovskite lattice seems to prevent the metal agglomeration during reduction steps [22,23]. Meanwhile, Pd incorporation via impregnation over the perovskite promotes its accessibility. Few studies made the comparison of both incorporation methods simultaneously. Zhou et al. [24] reported that Pd-supported  $La_{0.8}Fe_{0.2}CoO_3$  catalyst showed higher activity than the Pd-doped  $La_{0.8}Fe_{0.2}CoO_3$  catalyst in TWC due to the easier diffusion of palladium in the former. More recently, Rodríguez et al. [25] reported opposite results for  $LaFe_{0.65}Co_{0.3}Pd_{0.05}O_3$  and  $Pd/LaFe_{0.65}Co_{0.35}O_3$  in the same process due to the higher Pd dispersion in the active state.

To the best of the authors' knowledge, only Zhao et al. [26] compared  $Pd/La_{0.7}Sr_{0.3}CoO_3$  and  $La_{0.7}Sr_{0.3}Co_{0.95}Pd_{0.05}O_3$  catalysts for the NSR process. Non-supported or bulk perovskites were used in this study. They concluded that both methods improve significantly De- $NO_x$  activity of the perovskite-based catalysts, especially in the case of Pd-supported sample. However, no studies have been published regarding the comparison of both Pd incorporation methods over alumina-supported perovskites (30%  $La_{0.7}Sr_{0.3}CoO_3/Al_2O_3$ ). Furthermore, the effect of the Pd loading for both methods on the  $NO_x$  abatement has not been yet reported. Therefore, the main objective of this study is, for the first time in the literature, to optimize both, the Pd incorporation method and the Pd loading on 30%  $La_{0.7}Sr_{0.3}CoO_3/Al_2O_3$  samples for an efficient  $NO_x$  to  $N_2$  conversion.

A series of alumina supported perovskites with different Pd loadings were prepared by wetness impregnation and by doping the perovskite structure. The prepared samples were thoroughly characterized by a wide variety of physicochemical, spectroscopic and microscopy techniques, and tested for NO oxidation (NO-to- $NO_2$  conversion) and  $NO_x$  storage and reduction ( $NO_x$ -to- $N_2$  efficiency). In addition, the properties and catalytic behaviour of the novel formulations were further compared with a NSR model catalyst (1.5% Pt-15%  $BaO/Al_2O_3$ ).

## 2. Experimental

### 2.1. Perovskite-based samples preparation

Bulk perovskite  $La_{0.7}Sr_{0.3}CoO_3$  (LSCO) was prepared by the conventional citric acid method [27]. Firstly, appropriate amounts of La ( $(NO_3)_3 \cdot 6H_2O$  (Fluka, 99%), Co( $(NO_3)_2 \cdot 6H_2O$  (Sigma Aldrich, 98%) and Sr ( $(NO_3)_2$  (Sigma Aldrich, 99%) were dissolved in distilled water under vigorous stirring. Citric acid ( $C_6H_8O_7 \cdot H_2O$ , Sigma Aldrich, 99%) was then added as a complexing agent at a citrate to nitrate molar ratio of 1.1. The pH was adjusted to a value of 8 by an ammonia solution (25% as  $NH_3$ , Panreac). After solvent evaporation at 80 °C, the resulting gel was further dried at 120 °C overnight. The material was then calcined at 650 °C for 4 h under a flow of 5%  $O_2/He$  in order to achieve the perovskite structure.

Alumina supported perovskites were prepared by wetness impregnation method. Based on the results of a previous work [8], alumina supported samples were prepared with a perovskite nominal loading of 30 wt%. Initially,  $\gamma$ -alumina (SA6173, Saint Gobain) was precalcined at 700 °C for 4 h in static air. The perovskite precursors were then dissolved together with citric acid up to a concentration of 0.95 mol  $L^{-1}$ . The pH was adjusted again to a value of 8. The resulting solution was added to the alumina inside a rotary evaporator (under vacuum at 35 °C) to obtain a homogeneously distributed gel precursor over the alumina. Finally, the supported gel was calcined in 5%  $O_2/He$  following the same calcination procedure used for the bulk perovskite (up to 650 °C) to get the desired alumina supported perovskite 30%  $La_{0.7}Sr_{0.3}CoO_3/Al_2O_3$  (LSCO/ $Al_2O_3$ ).

"Pd-doped" samples were prepared by partial substitution of cobalt by palladium in the perovskite formulation. The Pd precursor, tetraamminepalladium (II) nitrate solution [ $Pd(NH_3)_4(NO_3)_2$ ], was dissolved in distilled water together with the precursors of La, Sr and Co. From here on, the preparation method was similar to the one above described for alumina-supported perovskites. The following samples with different Pd contents were synthesized: 30%  $La_{0.7}Sr_{0.3}Co_{0.95}Pd_{0.05}O_3/Al_2O_3$ , 30%  $La_{0.7}Sr_{0.3}Co_{0.89}Pd_{0.11}O_3/Al_2O_3$ , 30%  $La_{0.7}Sr_{0.3}Co_{0.84}Pd_{0.16}O_3/Al_2O_3$  and 30%  $La_{0.7}Sr_{0.3}Co_{0.78}Pd_{0.22}O_3/Al_2O_3$ . These Pd molar ratios correspond to nominal Pd loadings of 0.75, 1.5, 2.25 and 3.0 wt%, respectively. The general nomenclature adopted for the "Pd-doped" perovskites is LSCP(y)  $O/Al_2O_3$ , where "P" represents palladium and "y" the palladium molar ratio substituting Co (with y = 0.05, 0.11, 0.16 and 0.22).

"Pd-impregnated" samples were prepared by sequential incorporation of the same palladium loadings set for the Pd-doped samples (0, 0.75, 1.5, 2.25 and 3.0 wt%) over alumina-supported perovskite by wetness impregnation. Tetraamminepalladium (II) nitrate solution was used again as precursor, [ $Pd(NH_3)_4(NO_3)_2$ ]. The resulting samples were calcined at 500 °C for 4 h in static air. The following samples were synthesized: 0.75% Pd-LSCO/ $Al_2O_3$ , 1.5% Pd-LSCO/ $Al_2O_3$ , 2.25% Pd-LSCO/ $Al_2O_3$  and 3.0% Pd-LSCO/ $Al_2O_3$ .

A reference 2.0% Pd/ $Al_2O_3$  sample was prepared by wetness impregnation using  $\gamma$ -alumina (SA6173, Saint Gobain) precalcined at 700 °C for 4 h in static air. Nominal palladium loading of 2.0% was incorporated using tetraamminepalladium (II) nitrate solution as precursor, [ $Pd(NH_3)_4(NO_3)_2$ ]. After impregnation, the sample was calcined at 500 °C for 4 h in static air.

### 2.2. Preparation of the LNT model catalyst

This sample was prepared by the sequential incorporation of Pt and Ba over  $\gamma$ -alumina by wetness impregnation. First, appropriate amount of tetraammineplatinum(II) nitrate [ $Pt(NH_3)_4(NO_3)_2$ ] was dissolved into distilled water and added to the alumina in a rotatory evaporator. The process was repeated for barium using the adequate amount of barium acetate [ $Ba(CH_3COO)_2$ ]. The nominal weight loading of Pt and BaO was 1.5% and 15%, respectively. After each impregnation, the catalyst was calcined at 500 °C for 4 h.

### 2.3. Catalysts characterization

XRD diffraction patterns of the samples were obtained using a Philips PW1710 diffractometer. The samples were finely ground and subjected to Cu K $\alpha$  radiation in a continuous scan mode from 5° to 70° 2 $\theta$  with a 0.02° per second sampling interval. Data treatment was carried out using the PANalytical X'pert HighScore specific software.

Raman spectroscopy was performed at room temperature in the region of 250–750 cm<sup>-1</sup> using a LabRam HR (Horiba) spectrometer equipped with a CCD detector cooled at -75 °C. Measurements were carried out under microscope with a laser wavelength of 514.53 nm. A low dispersion grating of 1800 grooves/mm was chosen to get a maximum signal (to improve the resolution). The spectra were recorded and treated using the Labspec software (Horiba). Prior to the analysis, the instrument was calibrated using a silicon wafer.

Textural properties of the samples were determined by N<sub>2</sub> adsorption-desorption at 77 K, using the Micromeritics TriStar equipment. Pd, La, Sr, Al<sub>2</sub>O<sub>3</sub> and Co loadings were quantitatively determined by Inductively Coupled Plasma Optical Emission Spectroscopy, ICP-OES, using a Horiba Jobin Yvon Activa spectrometer. The solid samples were pre-reduced at 250 °C for 1 h and dissolved prior to the analysis.

The palladium dispersion was determined using the H<sub>2</sub> chemisorption method in a Micromeritics ASAP 2020system. The catalyst (0.2 g) was first outgassed at 350 °C for 3 h. Then, the sample was reduced in 50 mL min<sup>-1</sup> of 5% H<sub>2</sub>/Ar at 350 °C. After that, the sample was further outgassed at 350 °C to remove the residual hydrogen. The H<sub>2</sub> adsorption isotherm was recorded twice at 70 °C with an intermediate outgassing step. These conditions prevent palladium hydride formation, which could modify palladium dispersion value. The difference between both isotherms was linked to the H<sub>2</sub> chemisorbed on the catalyst surface.

The reducibility of the samples was investigated using the Micromeritics AutoChem II system. The quartz tube reactor was loaded with 0.1 g of sample and pretreated in 30 mL min<sup>-1</sup> of 5% O<sub>2</sub>/He mixture at 600 °C for 30 min. The samples were then heated from -10 °C to 950 °C with a temperature ramp of 10 °C min<sup>-1</sup> in a 5% H<sub>2</sub>/Ar mixture with a flowrate of 30 mL min<sup>-1</sup>. Water generated during the reduction was trapped using a cold trap. The gas stream was then analyzed by a TCD detector.

An Environmental Transmission Electron Microscope (ETEM) was used to visualize the nano-structure of the selected catalysts after reduction at 250 °C for 1 h. This latest generation ETEM (Titan 80–300 kV from FEI™) was equipped with an imaging aberration corrector and an energy-dispersive X-ray (EDX) analyzer (SDD X-Max 80 mm<sup>2</sup> from Oxford Instruments™) used for elemental chemical analysis. The sample was deposited on titania grids covered with a silica film and placed into a Gatan™ furnace-type holder. The ETEM was operated with a beam voltage at 80 and 300 kV to evaluate the effect of the electron beam energy.

Pd different oxidation states and surface content was analyzed using X-ray photoelectronic spectroscopy (XPS). The analysis was carried out in a SPECS electron spectrometer with a Phoibos 150 1D-DLD energy analyzer using Al-K $\alpha$  (1486.7 eV) radiation source. To obtain the XPS spectra, the pressure of the analysis chamber was maintained at 5 × 10<sup>-10</sup> mbar. The binding energy (BE) scale was adjusted by setting the C 1s transition at 284.6 eV.

### 2.4. Catalytic activity

The catalytic tests were carried out using a total flow rate of 2 L min<sup>-1</sup> (GHSV = 123,500 h<sup>-1</sup>) and a catalyst grain size of 0.3–0.5 mm. These experimental conditions guaranteed the absence of external and internal mass transfer limitations [7].

The outlet gas composition was continuously measured using a MKS MultiGas 2030 FT-IR analyzer linked to a MKS Cirrus quadrupole MS. NO, NO<sub>2</sub>, NH<sub>3</sub>, N<sub>2</sub>O and H<sub>2</sub>O were quantitatively monitored by the FT-IR analyzer, whereas H<sub>2</sub>, N<sub>2</sub> and O<sub>2</sub> were qualitatively monitored by the

MS analyzer.

#### 2.4.1. NO-to-NO<sub>2</sub> oxidation activity ( $X_{\text{NO-to-NO}_2}$ )

NO oxidation tests were carried out in a vertical stainless steel reactor filled with 0.5 g of catalyst inside a 3-zone tube furnace. The feed stream composition was: 500 ppm NO, 6% O<sub>2</sub> and Ar as the balance gas. Stable NO and NO<sub>2</sub> signals were observed once the steady state was reached at each temperature (~ 20 min after the temperature was stabilized). Eq. (1) was used in order to calculate the NO-to-NO<sub>2</sub> conversion values.

$$X_{\text{NO-to-NO}_2}(\%) = \frac{F_{\text{NO}}^{\text{in}} - F_{\text{NO}}^{\text{out}}}{F_{\text{NO}}^{\text{in}}} \times 100 \quad (1)$$

where  $F_{\text{NO}}^{\text{in}}$  is the NO inlet molar flow (μmol min<sup>-1</sup>) and  $F_{\text{NO}}^{\text{out}}$  is the outlet NO molar flow (μmol min<sup>-1</sup>).

#### 2.4.2. NO<sub>x</sub> storage and reduction (NSR) experiments

The same reaction system was used than for NO oxidation. During the lean period (150 s), the feed composition was: 500 ppm NO, 6% O<sub>2</sub> and Ar as the carrier gas. During the rich period (20 s), oxygen was replaced by hydrogen at a concentration of 3%. Gases were fed via mass flow controllers. Temperature was continuously monitored by means of a thermocouple inside the catalytic bed. The catalytic activity was evaluated in terms of the parameters listed below.

**NO<sub>x</sub> storage capacity (NSC):** percentage of NO<sub>x</sub> stored during the lean period as a function of the amount of NO at the inlet (Eq. (2)).

$$\text{NSC}(\%) = \frac{F_{\text{NO}}^{\text{in}} t_L - \int_0^{t_L} F_{\text{NO}_x}^{\text{out}} dt}{F_{\text{NO}}^{\text{in}} t_L} \times 100 \quad (2)$$

where  $F_{\text{NO}_x}^{\text{out}}$  is the NO<sub>x</sub> outlet molar flow (μmol min<sup>-1</sup>) and  $t_L$  (min) is the duration of the lean cycle.

**NO global conversion ( $X_{\text{NO}}$ ):** percentage of NO converted during the whole operation (lean and rich cycles) with respect to the total amount of NO fed (Eq. (3)),

$$X_{\text{NO}}(\%) = \frac{F_{\text{NO}}^{\text{in}} (t_L + t_R) - \int_0^{t_L+t_R} F_{\text{NO}}^{\text{out}} dt}{F_{\text{NO}}^{\text{in}} (t_L + t_R)} \times 100 \quad (3)$$

where  $t_R$  (min) is the duration of the rich cycle.

**Yield of N-compounds ( $Y_{\text{NO}_2}$ ,  $Y_{\text{NH}_3}$ ,  $Y_{\text{N}_2\text{O}}$ ,  $Y_{\text{N}_2}$ ):** defined as the mole % of the corresponding component at the outlet in relation to NO amount at the inlet, i.e.

$$Y_{\text{NO}_2}(\%) = \frac{\int_0^{t_L+t_R} F_{\text{NO}_2}^{\text{out}} dt}{F_{\text{NO}}^{\text{in}} (t_L + t_R)} \times 100 \quad (4)$$

$$Y_{\text{NH}_3}(\%) = \frac{\int_0^{t_L+t_R} F_{\text{NH}_3}^{\text{out}} dt}{F_{\text{NO}}^{\text{in}} (t_L + t_R)} \times 100 \quad (5)$$

$$Y_{\text{N}_2\text{O}}(\%) = \frac{\int_0^{t_L+t_R} 2F_{\text{N}_2\text{O}}^{\text{out}} dt}{F_{\text{NO}}^{\text{in}} (t_L + t_R)} \times 100 \quad (6)$$

$$Y_{\text{N}_2}(\%) = \frac{\int_0^{t_L+t_R} 2F_{\text{N}_2}^{\text{out}} dt}{F_{\text{NO}}^{\text{in}} (t_L + t_R)} \times 100 \quad (7)$$

where  $F_{\text{NH}_3}^{\text{out}}$ ,  $F_{\text{N}_2\text{O}}^{\text{out}}$  and  $F_{\text{N}_2}^{\text{out}}$  are the molar flow (μmol min<sup>-1</sup>) of NH<sub>3</sub>, N<sub>2</sub>O and N<sub>2</sub> at the outlet, respectively.

## 3. Results and discussion

### 3.1. Characterization

Fig. 1a shows the XRD patterns of the alumina supported perovskites with palladium nominal loadings of 0.75, 1.5 and 3.0 wt% incorporated by impregnation or by cobalt partial substitution in the perovskite formulation. Diffractograms of bulk perovskite (LSCO),

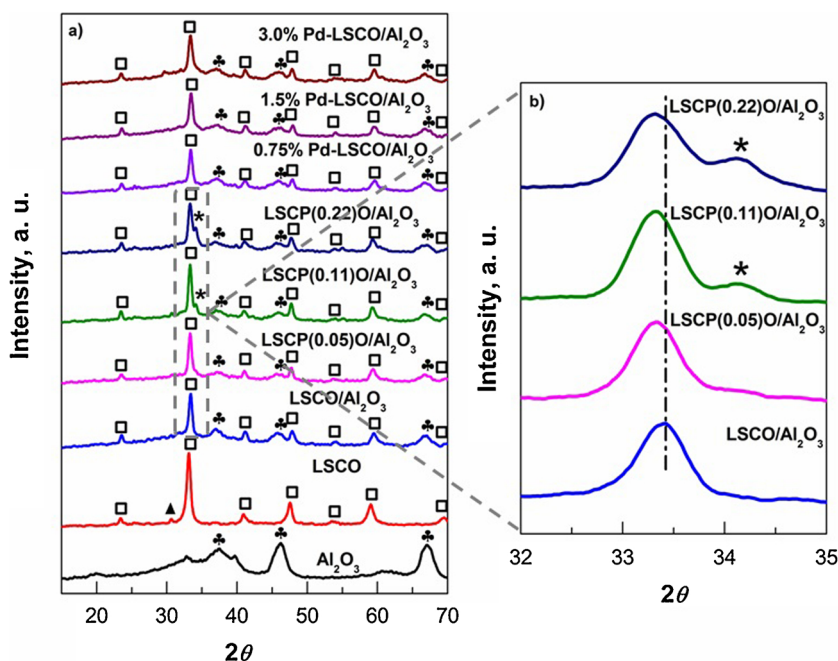


Fig. 1. XRD diffractograms of: a) alumina ( $\text{Al}_2\text{O}_3$ ), bulk perovskite (LSCO) and alumina-supported perovskites with increasing palladium loadings incorporated by: impregnation ( $y\%$  Pd-LSCO/ $\text{Al}_2\text{O}_3$ ) or doping (LSCP( $y$ )/ $\text{Al}_2\text{O}_3$ ), and b) enlargement of the specific zone from  $32$  to  $35^\circ$   $2\theta$  of Fig. 1a. Symbol \* corresponds to PdO,  $\clubsuit$  to  $\text{Al}_2\text{O}_3$ ,  $\blacktriangle$  to  $\text{SrCO}_3$  and  $\square$  to  $\text{La}_{0.7}\text{Sr}_{0.3}\text{CoO}_3$  phases.

Table 1

The textural properties of alumina supported perovskite with increasing Pd loads incorporated by impregnation or doping, along with the corresponding to alumina support ( $\gamma\text{-Al}_2\text{O}_3$ ) and  $\text{La}_{0.7}\text{Sr}_{0.3}\text{CoO}_3$  perovskite (LSCO).

Sample	$S_{\text{BET}}$ , $\text{m}^2 \text{g}^{-1}$	$V_p$ , $\text{cm}^3 \text{g}^{-1}$	$d_c$ , nm
$\gamma\text{-Al}_2\text{O}_3$	186.5	0.63	
LSCO/ $\text{Al}_2\text{O}_3$	122.1	0.41	12
LSCP(0.05)O/ $\text{Al}_2\text{O}_3$	107.4	0.32	12
LSCP(0.11)O/ $\text{Al}_2\text{O}_3$	109.0	0.32	13
LSCP(0.16)O/ $\text{Al}_2\text{O}_3$	110.5	0.34	13
LSCP(0.22)O/ $\text{Al}_2\text{O}_3$	108.9	0.32	12
0.75% Pd-LSCO/ $\text{Al}_2\text{O}_3$	122.3	0.39	12
1.5% Pd-LSCO/ $\text{Al}_2\text{O}_3$	121.5	0.38	12
2.25% Pd-LSCO/ $\text{Al}_2\text{O}_3$	121.0	0.39	12
3.0% Pd-LSCO/ $\text{Al}_2\text{O}_3$	116.9	0.38	12
LSCO	24.3	0.12	17

alumina-supported perovskite (LSCO/ $\text{Al}_2\text{O}_3$ ) and alumina ( $\text{Al}_2\text{O}_3$ ), are also included as reference. Alumina supported perovskites show characteristic diffraction peaks of a highly disordered cubic alumina with low crystallinity ( $\clubsuit$ ) together with a highly crystallized perovskite ( $\square$ ). As already reported in a previous work [8], the perovskite agglomeration during the high temperature calcination step is partially inhibited due to its distribution over the alumina surface [28]. Consequently, the crystal size of the 30% LSCO/ $\text{Al}_2\text{O}_3$  sample estimated by Scherrer equation is 12–13 nm, whereas the crystal size of the bulk variant is larger, i.e. 17 nm (Table 1). Besides the perovskite phase, a weak  $\text{SrCO}_3$  diffraction peak was also detected at  $2\theta = 30.5^\circ$  ( $\blacktriangle$ ) for bulk perovskite. This peak disappears for the supported samples, probably due to a  $\text{SrCO}_3$  higher dispersion.

Pd or PdO peaks were absent for Pd-impregnated samples due to the small particle size and/or low metal content [14,17]. In contrast, the enlargement made for the specific zone of  $32\text{--}35^\circ$   $2\theta$  for Pd-doped samples (Fig. 1b) exhibits an additional peak (\*) at  $2\theta \sim 34.1^\circ$ , characteristic of tetragonal palladium oxide ( $33.837^\circ$   $2\theta$ , PDF-00-041-1107) [24]. The intensity of PdO diffraction peak increases with palladium content. This unequivocally reveals that palladium is not fully accommodated within the perovskite lattice for Pd-doped samples. Indeed, once the capacity to accommodate Pd in the lattice is fulfilled, Pd is preferentially segregated to the surface and detected by XRD. Meanwhile, the main diffraction peak of the perovskite ( $33.5^\circ$ ) is slightly

displaced to lower angles (around  $0.1^\circ$ ) for the Pd doped samples, regardless the Pd loading. This fact could be attributed to the expansion of the perovskite lattice due to  $\text{Co}^{3+}$  partial substitution by  $\text{Pd}^{n+}$  cation with larger ionic diameter [29,30].

Fig. 2 shows the Raman spectra for the samples containing 0.75 wt% of Pd incorporated by impregnation and doping. Several bands attributed to  $\text{Co}_3\text{O}_4$  are identified at  $483$ ,  $525$ ,  $623$  and  $692 \text{ cm}^{-1}$  in both samples [31]. Raman bands attributed to PdO are detected at  $276$ ,  $441$  and  $646 \text{ cm}^{-1}$  for the sample prepared by Pd doping [32,33]. On the

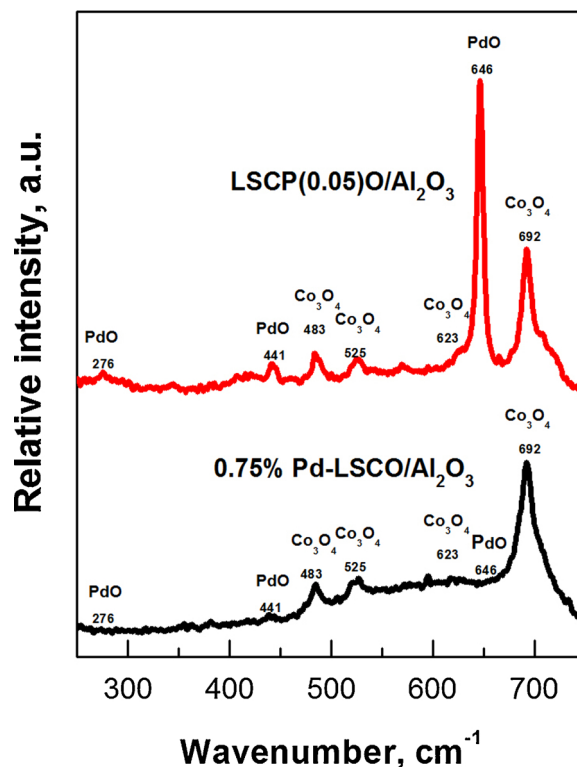


Fig. 2. Raman spectra and phase identification of LSCP(0.05)O/ $\text{Al}_2\text{O}_3$  and 0.75% Pd-LSCO/ $\text{Al}_2\text{O}_3$  catalysts.



contrary, the signal intensity of those bands is negligible for the sample prepared by Pd impregnation due to lower crystal domain of PdO, as it will be further verified by TEM/STEM images.

Thus, experimental evidences suggest that two different Pd species coexist in the Pd-doped samples; the ones accommodated within the perovskite lattice as evidenced by the displacement of the main diffraction peak of the perovskite by XRD, and segregated large PdO particles easily detectable by Raman. On the other hand, the absence of Raman bands attributed to PdO indicates that Pd particles are small and well dispersed in the case of samples prepared by impregnation.

The main textural properties of the alumina support, bulk perovskite and Pd-impregnated and Pd-doped samples were determined by N<sub>2</sub> adsorption/desorption isotherms. Table 1 shows the specific surface areas (SSA) and pore volumes (V<sub>p</sub>) for all the samples above described in the experimental section. SSA of bare alumina and bulk perovskite was 186.5 m<sup>2</sup> g<sup>-1</sup> and 24.3 m<sup>2</sup> g<sup>-1</sup>, respectively. As expected, the incorporation of LSCO on the alumina support (LSCO/Al<sub>2</sub>O<sub>3</sub>) led to a significant decrease of the surface area (122.1 m<sup>2</sup> g<sup>-1</sup>) and pore volume (0.41 cm<sup>3</sup> g<sup>-1</sup>), due to the partial occupation of its pores by the perovskite phase. The incorporation of Pd by impregnation does not modify importantly the SSA of the LSCO/Al<sub>2</sub>O<sub>3</sub> sample. However, the SSA and V<sub>p</sub> of Pd-doped samples were slightly lower than that observed for the Pd-impregnated counterparts. It seems that the large PdO particles present in these samples, as observed by XRD and Raman, could contribute to the partial occupation of the pores of the support.

The distribution of La, Co, Sr, Al and Pd at the nanoscale and the morphology of the samples were observed by TEM/STEM-EDX analysis. STEM images and the corresponding EDX mapping of Pd and La for the samples with 0.75 wt% of Pd incorporated by wetness impregnation and doping are shown in Fig. 3. The EDX mapping was used to evaluate the distribution of the perovskite over the alumina. In general, a well dispersed perovskite phase over the alumina is observed, with La homogeneously distributed over the sampling area, as in Fig. 3b. Besides, some areas where the perovskite is concentrated were also observed, evidenced by La rich domains in EDX, as in Fig. 3a. The distribution of the perovskite over alumina is not influenced by the Pd incorporation method.

Focusing on the Pd distribution, small spherical particles homogeneously distributed over the alumina and perovskite surface can be observed for the sample prepared by impregnation (Fig. 3a). Besides, the size of the Pd particles was around 2–3 nm as identified by STEM images (Figure S1a). On the other hand, Pd distribution was not homogeneous in the sample prepared by doping. Pd rich areas forming larger nanoparticles can be easily identified in Fig. 3b. The size of the Pd particles was around 5–12 nm as identified by STEM images (Figure S1b). Furthermore, TEM-EDX experiments (Figure S2) revealed the presence of Pd even if in the sample some areas without any Pd nanoparticles exist, confirming that part of Pd was incorporated in the perovskite lattice.

The higher size of palladium particles for Pd-doped samples is probably due to the exposure of the metallic phase to a higher calcination temperature (650 °C) during the perovskite structure crystallization. Besides, nitrates decomposition during the calcination step could result in the formation of hot-spots [7] that would probably further increase the local temperature above 650 °C, leading to palladium particles aggregation. On the other hand, the incorporation of Pd by impregnation once the perovskite structure was conformed over the alumina support (LSCO/Al<sub>2</sub>O<sub>3</sub>), allowed to control and fix the calcination temperature at 500 °C, inhibiting the aggregation of the palladium particles and leading to smaller Pd particles.

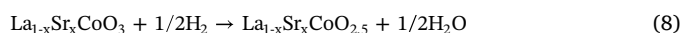
Table 2 shows the Pd loading (according to ICP-OES), the metal dispersion (determined by H<sub>2</sub> chemisorption), as well as Pd 3d BE position and Pd/La atomic ratio (determined by XPS). Regarding the Pd loading, as expected, it increased proportionally close to the nominal values for both preparation methods. The palladium dispersion progressively decreases while increasing the metal content due to its

progressive agglomeration. Samples prepared by doping the perovskite showed significantly lower palladium dispersion values than Pd-impregnated counterparts. The fact that some Pd is incorporated in the perovskite lattice along with the larger nanoparticles observed by TEM/STEM explain the low dispersion value for Pd-doped samples. On the other hand, the homogeneous distribution of Pd over alumina and perovskite surface favours a high dispersion for Pd-impregnated samples.

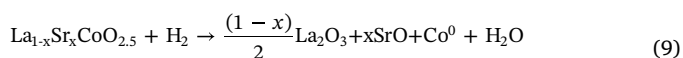
XPS spectra of Pd 3d core level of the samples with 1.5 and 3.0 wt% of palladium incorporated by both methods were acquired (Fig. 4). The typical binding energy (BE) values for metallic palladium (Pd<sup>0</sup>) is reported to be around 335.5 eV [19,34], whereas Pd<sup>2+</sup> characteristic BE is observed at slightly higher values, around 336.7 ± 0.3 eV [14,22,24,34,35]. Pd 3d<sub>5/2</sub> transition is observed at 337.0 eV (Table 2) for Pd-impregnated samples, revealing that the main palladium species are Pd<sup>2+</sup> forming small PdO clusters on the surface [36,37]. Pd 3d<sub>5/2</sub> transition for the reference 2.0% Pd/Al<sub>2</sub>O<sub>3</sub> formulation (Figure S3) was placed at lower BE values, i.e. 336.0 eV, closer to that reported for metallic palladium. These results reveal that the perovskite strongly interacts with the Pd particles and promotes their oxidation [38]. On the other hand, Pd-doped samples show a BE position (336.0 eV) closer to the characteristic position of Pd<sup>0</sup>. This fact could be attributed to the palladium particles partial auto-reduction derived from the exposure at high temperatures during the calcination step [39]. Indeed, it has been found that the sudden temperature raise during self-propagating combustion process can exceed the decomposition temperature of PdO (~800 °C) [15,40], leading to the formation of surface Pd<sup>0</sup>.

Pd/La atomic ratio, estimated from the Pd 3d and La 3d relative data, are summarized in Table 2. Lower Pd/La ratios were observed for Pd-doped samples, in good agreement with the palladium partial accommodation within the lattice. It is worth noting that the differences in Pd/La ratios between the samples prepared by both methods are higher for lower palladium contents. The Pd-doped and Pd-impregnated samples with a 1.5% of palladium nominal loading show a Pd/La ratio of 0.07 and 0.14, respectively. The partial incorporation of Pd in the perovskite lattice reduces the superficial content of the noble metal for Pd-doped samples and results in a lower Pd/La ratio. On the other hand, the samples with higher Pd content (3%) show closer Pd/La ratios of 0.15 and 0.18, respectively. It seems that the perovskite presents a limited capacity to accommodate palladium within its lattice, and once saturated, Pd particles are segregated to the surface.

Hydrogen consumption profiles, normalized according to the perovskite mass, were determined by temperature programmed reduction experiments. H<sub>2</sub>-TPR profiles for Pd-impregnated and Pd-doped samples are shown in Fig. 5a and b, respectively. LSCO, LSCO/Al<sub>2</sub>O<sub>3</sub>, CoAl<sub>2</sub>O<sub>4</sub> and 2% Pd/Al<sub>2</sub>O<sub>3</sub> reference profiles are also shown in Fig. 5c for further comparison. As already reported in previous works [7,8], the H<sub>2</sub>-TPR profile of the bulk La<sub>0.7</sub>Sr<sub>0.3</sub>CoO<sub>3</sub> (LSCO) sample shows two main H<sub>2</sub> consumption regions: one below and one above 450 °C. H<sub>2</sub> consumption below 450 °C is assigned to the reduction of oxygen chemisorbed on the catalyst surface, and the progressive reduction of Co<sup>3+</sup> to Co<sup>2+</sup> from the surface to the inner layers, for maintaining the perovskite electroneutrality and structure [41–43],



Whereas, the hydrogen consumption at higher temperature is linked to the final reduction of Co<sup>2+</sup> to Co<sup>0</sup>, again beginning from the surface and progressing to the bulk sample.



Finally, hydrogen consumption above 700 °C is due to surface decomposition of residual carbonates in the form of CO<sub>2</sub> [44].

30% La<sub>0.7</sub>Sr<sub>0.3</sub>CoO<sub>3</sub>/Al<sub>2</sub>O<sub>3</sub> sample exhibits two main differences with respect to the LSCO bulk sample (Fig. 5c). On the one hand, the peaks previously assigned to the reduction of the surface species, widen

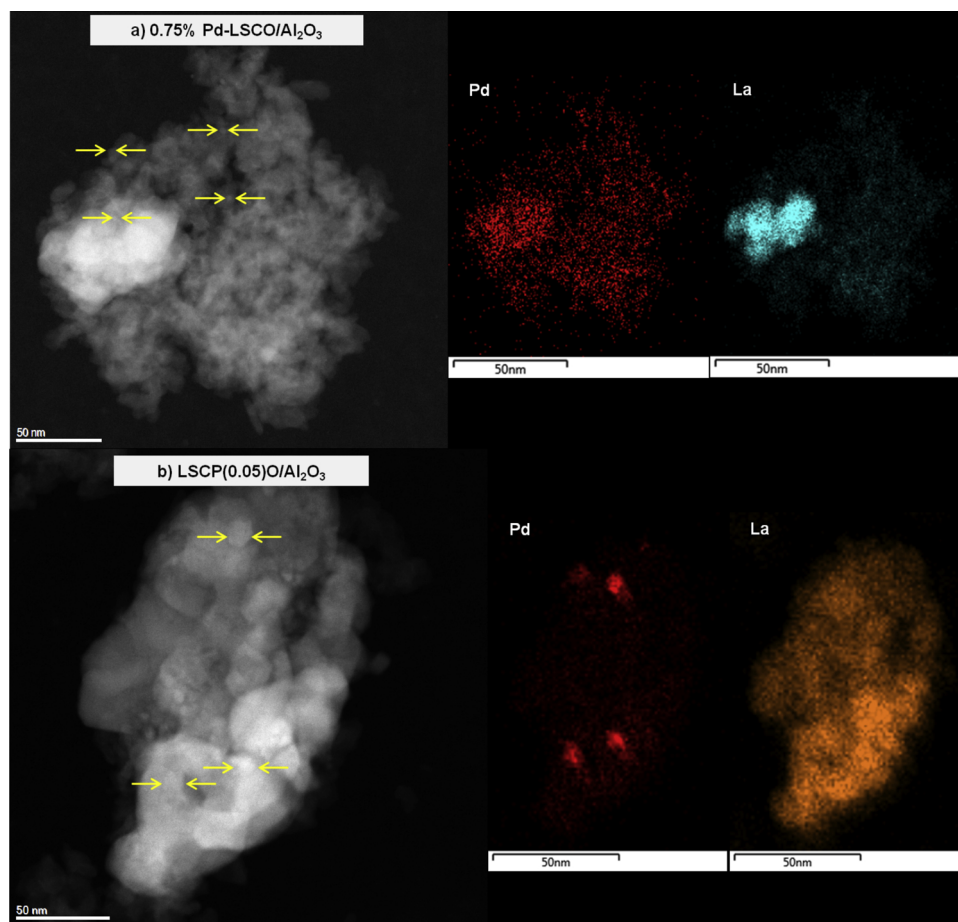


**Fig. 3.** STEM images and the corresponding EDX analysis mapping of the samples with a 0.75 wt% of Pd incorporated by: a) wetness impregnation over supported perovskite or b) doping perovskite structure.

**Table 2**

Pd loading and dispersion along with Pd 3d BE position and surface content obtained for the samples with increasing Pd contents incorporated by impregnation or doping.

Sample	Pd, %	Pd <sub>disp.</sub> , %	Pd 3d <sub>5/2</sub> , eV	Pd/La (atomic ratio)
2.0% Pd/Al <sub>2</sub> O <sub>3</sub>	1.84	26.3	336.0	–
LSCP(0.05)O/Al <sub>2</sub> O <sub>3</sub>	0.73	12.0	–	–
LSCP(0.11)O/Al <sub>2</sub> O <sub>3</sub>	1.36	6.6	336.0	0.07
LSCP(0.16)O/Al <sub>2</sub> O <sub>3</sub>	2.15	5.9	–	–
LSCP(0.22)O/Al <sub>2</sub> O <sub>3</sub>	2.65	4.4	336.1	0.15
0.75% Pd-LSCO/Al <sub>2</sub> O <sub>3</sub>	0.65	39.3	–	–
1.5% Pd-LSCO/Al <sub>2</sub> O <sub>3</sub>	1.16	31.4	337.0	0.14
2.25% Pd-LSCO/Al <sub>2</sub> O <sub>3</sub>	1.83	23.2	–	–
3.0% Pd-LSCO/Al <sub>2</sub> O <sub>3</sub>	2.39	22.1	337.0	0.18

and displace to lower temperatures. This fact could be attributed to the enhanced perovskite reducibility due to its high dispersion over the alumina surface. On the other hand, a new H<sub>2</sub> consumption above 800 °C is observed due to the reduction of cobalt species in the form of cobalt aluminate (CoAl<sub>2</sub>O<sub>4</sub>) [45,46].

The hydrogen consumption profile is significantly altered after palladium incorporation. Pd-doped and Pd-impregnated samples show four main reduction regions: below 75 °C, 75 °C–225 °C, 225 °C–500 °C and above this temperature. In agreement with the TPR spectrum of 2.0% Pd/Al<sub>2</sub>O<sub>3</sub> sample (Fig. 5c), the first peak centered around 23 °C is assigned to the reduction of isolated PdO<sub>x</sub> species [47]. The second peak, centered around 150 °C is attributed to the reduction of cobalt and palladium in close contact. Note that the H<sub>2</sub>/Pd ratios estimated from the hydrogen consumption of the first peak are lower than 1

(Table 3). Taking into account that palladium reduction stoichiometry reveals that 1 mol of H<sub>2</sub> is needed to reduce 1 mol of PdO, the remaining Pd should be reduced in this temperature region. Then the third reduction peak, centered around 350 °C, is linked to the reduction of the remaining Co within the perovskite structure [17,48]. The peak above 500 °C is ascribed to the final reduction of Co<sup>2+</sup> inside the alumina matrix in the form of cobalt aluminate (CoAl<sub>2</sub>O<sub>4</sub>). Therefore, the modification of the H<sub>2</sub>-TPR patterns denotes that the reduction of Co<sup>3+</sup> and Co<sup>2+</sup> occurs at significantly lower temperatures with respect to 30% La<sub>0.7</sub>Sr<sub>0.3</sub>CoO<sub>3</sub>/Al<sub>2</sub>O<sub>3</sub> sample. This suggests that the incorporation of Pd promotes the reducibility of the Co species due to the hydrogen dissociation and activation at the surface of Pd<sup>0</sup> and its subsequent spillover to Co sites [9,17,22,24,49,50].

Some differences were observed in the reduction profiles of Pd-based samples prepared by doping or impregnation (Fig. 5a and b). Firstly, the peak situated at the lowest temperature, previously assigned to the reduction of isolated PdO<sub>x</sub> particles, is more pronounced for the Pd-doped samples. In fact, the corresponding H<sub>2</sub> consumption increases from values between 11–177 μmol H<sub>2</sub> g<sup>−1</sup> for Pd-impregnated samples to values 38–208 μmol H<sub>2</sub> g<sup>−1</sup> for Pd-doped samples (Table 3). Meanwhile, the second reduction peak ascribed to the simultaneous reduction of Pd and Co in close contact follows the opposite trend (Table 3). These results reveal that the weaker interaction between PdO and perovskite facilitates the reduction of Pd, and limits the hydrogen spillover from the Pd to the perovskite [24,51]. It is worth to mention that the reduction of Co species in the perovskite framework takes place at lower temperature for Pd-doped samples with low Pd content. This fact denotes that the palladium partial accommodation within the lattice promotes the reduction of adjacent Co inside the structure due to

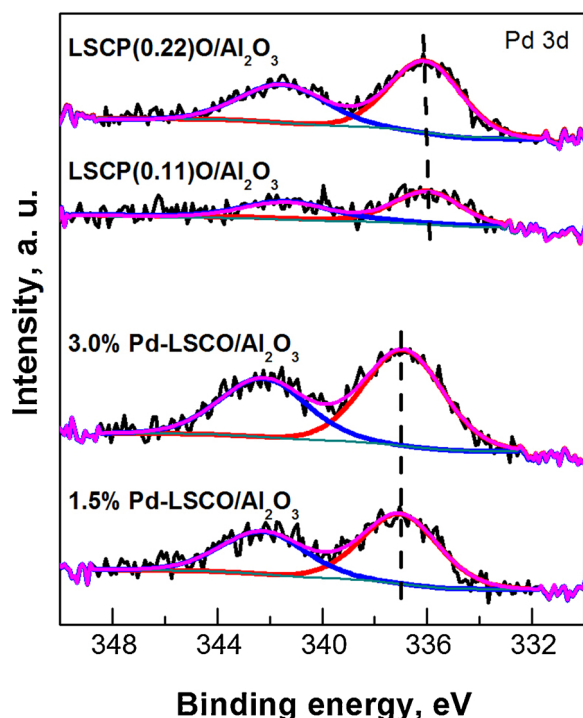


Fig. 4. XPS spectra of Pd 3d of the samples with palladium nominal loadings of 1.5 and 3 wt% incorporated by: wetness impregnation over supported perovskite (1.5% Pd-LSCO/Al<sub>2</sub>O<sub>3</sub> and 3.0% Pd-LSCO/Al<sub>2</sub>O<sub>3</sub>) or doping perovskite structure (LSCP(0.11)O/Al<sub>2</sub>O<sub>3</sub> and LSCP(0.22)O/Al<sub>2</sub>O<sub>3</sub>).

higher proximity of both phases [24].

### 3.2. Catalytic experiments

NO-to-NO<sub>2</sub> conversion ( $X_{\text{NO-to-NO}_2}$ ) was measured at different temperatures (Fig. 6) for the alumina-supported perovskite-based samples with increasing palladium loadings (i.e., 0, 0.75, 1.5 and 3.0 wt%) incorporated by impregnation or doping methods. The activity for the NSR model catalyst is also included as reference. As previously reported [7,8], NO conversion initially increased with the reaction temperature in the kinetically controlled regime up to 350 °C. Then, at higher temperatures, the NO-to-NO<sub>2</sub> conversion decreased with temperature due to thermodynamic restrictions as usual for exothermic reactions. Pd-

based formulations show similar  $X_{\text{NO-to-NO}_2}$  compared to that of the reference LSCO/Al<sub>2</sub>O<sub>3</sub> sample, indicating that the perovskite itself is the main catalytic material to catalyze the NO oxidation with a low contribution of Pd sites [52]. In agreement with the reported by Irfan et al. [53], the presence of nanoparticles of Co<sub>3</sub>O<sub>4</sub> well-dispersed on the surface accelerates NO oxidation. Among them, Pd-doped samples show slightly lower NO oxidation capacity due to the partial overlap of Co<sub>3</sub>O<sub>4</sub> and perovskite phases derived from the lower dispersion of the palladium phase, as observed in the characterization section. Perovskite-based formulations significantly promote the NO oxidation with respect to Pt-based model catalyst (1.5% Pt-15%BaO/Al<sub>2</sub>O<sub>3</sub>). This confirms the potential of the developed materials as efficient alternative to promote the NO oxidation reactions in automotive catalysis [7,8,12].

Fig. 7 shows the evolution of NO, NO<sub>2</sub>, NO<sub>x</sub>, NH<sub>3</sub> and N<sub>2</sub>O outlet concentration, as well as MS signal of N<sub>2</sub> at 400 °C, for two consecutive lean and rich cycles. Reference LSCO/Al<sub>2</sub>O<sub>3</sub> catalyst (Fig. 7a) and the samples with a 1.5 wt% of palladium incorporated by impregnation (Fig. 7b) or by cobalt partial substitution (Fig. 7c) were assessed. The lowest NO, NO<sub>2</sub> and NO<sub>x</sub> outlet concentrations were observed during the beginning of the lean period due to NO<sub>x</sub> adsorption on the trapping sites of the perovskite. This process occurs via NO<sub>2</sub> adsorption over alumina support, and especially over the basic storage components (SrO and La<sub>2</sub>O<sub>3</sub>) or over surface oxygen vacancies of the perovskite [18,54,55]. NO adsorption through the disproportionation reaction forms a nitrate and releases one molecule of NO [56]. The NO concentration at the reactor outlet increases with increasing the duration of the lean period due to the saturation of the storage sites. Shaded areas in Fig. 7 are related with the NO<sub>x</sub> storage capacity of the samples, i.e. the higher the shaded area, the higher the storage capacity is. After 150 s, the rich period begins by admitting H<sub>2</sub> to the reactor, which causes the release of the stored NO<sub>x</sub> and their reduction. However, some of the NO<sub>x</sub> stored is released without being converted, which denotes a faster rate for nitrates decomposition than for NO<sub>x</sub> reduction [57] at 400 °C. The NO<sub>x</sub> reduction process is strongly affected by the presence of the noble metal. Indeed, NO<sub>x</sub> concentration reached 2000 ppm in the absence of Pd, whereas NO<sub>x</sub> concentration peaks achieved lower values, i.e. 920 and 1450 ppm for Pd-impregnated and Pd-doped samples, respectively. Besides, at the end of the rich period, Pd-based samples reached almost zero NO<sub>x</sub> level, which is indicative of a deep reduction process. On the contrary, 50 ppm of NO remained unreduced in the effluent of the reactor in the absence of Pd.

In order to gain more insight into the NO reduction, additional experiments were carried out under steady state between 135 °C and 450 °C, feeding 500 ppm of NO and 0.5% H<sub>2</sub> and results are collected in

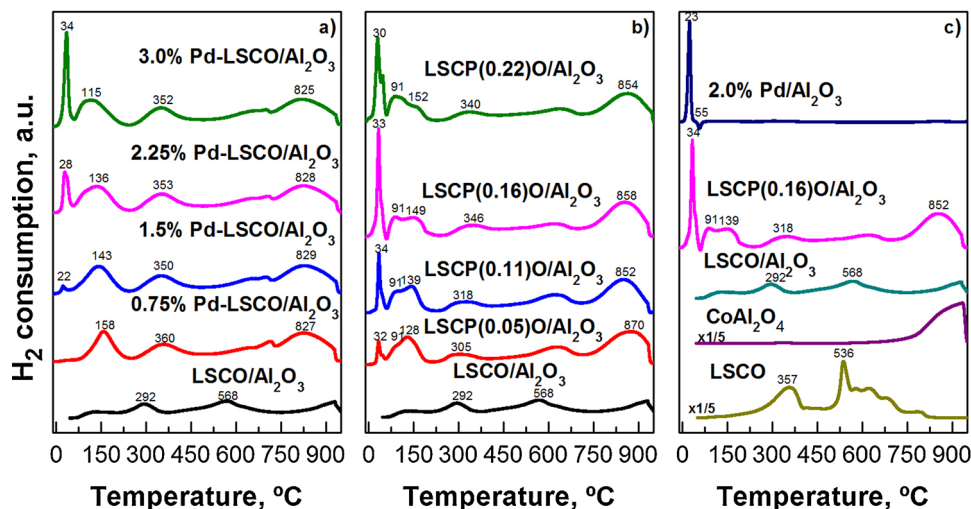


Fig. 5. H<sub>2</sub>-TPR profiles normalized per sample mass of: a) Pd-impregnated samples, b) Pd-doped samples and c) reference samples (La<sub>0.7</sub>Sr<sub>0.3</sub>CoO<sub>3</sub> perovskite (LSCO), CoAl<sub>2</sub>O<sub>4</sub>, 30% La<sub>0.7</sub>Sr<sub>0.3</sub>CoO<sub>3</sub>/Al<sub>2</sub>O<sub>3</sub> (30% LSCO/Al<sub>2</sub>O<sub>3</sub>) and 2.0% Pd/Al<sub>2</sub>O<sub>3</sub> samples).



**Table 3**

Deconvoluted hydrogen consumption related to different reduction steps for supported perovskites with increasing palladium incorporated by impregnation or by doping.

Sample	PdO→Pd <sup>0a</sup> , μmol H <sub>2</sub> g <sup>-1</sup>	PdO-Co <sup>b</sup> , μmol H <sub>2</sub> g <sup>-1</sup>	Co <sup>+3</sup> →Co <sup>0c</sup> , μmol H <sub>2</sub> g <sup>-1</sup>	CoAl <sub>2</sub> O <sub>4</sub> <sup>d</sup> , μmol H <sub>2</sub> g <sup>-1</sup>	Total H <sub>2</sub> consumption, μmol H <sub>2</sub> g <sup>-1</sup>	H <sub>2</sub> /Pd <sup>f</sup>
LSCO/Al <sub>2</sub> O <sub>3</sub>	–	–	820	466	1286	–
LSCP(0.05)O/Al <sub>2</sub> O <sub>3</sub>	38	335	169	1172	1694	0.64
LSCP(0.11)O/Al <sub>2</sub> O <sub>3</sub>	101	335	210	1115	1761	0.91
LSCP(0.16)O/Al <sub>2</sub> O <sub>3</sub>	180	300	217	1076	1772	0.97
LSCP(0.22)O/Al <sub>2</sub> O <sub>3</sub>	208	300	258	1034	1829	0.96
0.75% Pd-LSCO/Al <sub>2</sub> O <sub>3</sub>	11	339	375	1050	1775	0.21
1.5% Pd-LSCO/Al <sub>2</sub> O <sub>3</sub>	33	384	363	1039	1820	0.35
2.25% Pd-LSCO/Al <sub>2</sub> O <sub>3</sub>	110	402	355	1012	1879	0.74
3.0% Pd-LSCO/Al <sub>2</sub> O <sub>3</sub>	177	366	331	1011	1885	0.91
2.0% Pd/Al <sub>2</sub> O <sub>3</sub>	152	–	–	–	–	–

<sup>e</sup>Sum of all integrated peaks.

<sup>a</sup> Integration of peak centered around 30 °C.

<sup>b</sup> Integrated peak centered around 100–150 °C.

<sup>c</sup> Integrated peak centered around 300–350 °C.

<sup>d</sup> Sum of integrated peaks centered above 600 °C.

<sup>f</sup> Hydrogen consumption in the first peak related to Pd content in the sample.

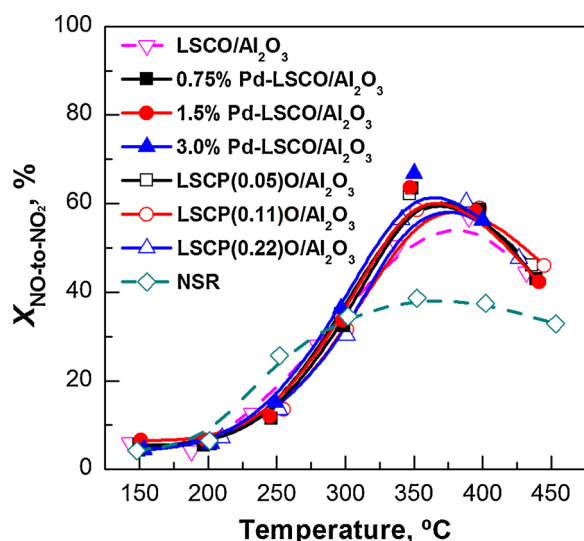


**Fig. 6.** NO-to-NO<sub>2</sub> oxidation capacity ( $X_{\text{NO-to-NO}_2}$ ) of alumina supported perovskite without Pd (LSCO/Al<sub>2</sub>O<sub>3</sub>) and this sample with a 0.75, 1.5% and 3.0% Pd incorporated by impregnation (solid symbols) or by doping (hollow symbols).

Tables S1–S3. In the absence of Pd, the LSCO/Al<sub>2</sub>O<sub>3</sub> sample showed an incomplete NO reduction below 300 °C, while the NO reduction was almost complete in all the studied temperature range for Pd-based samples. The higher NO reduction performance for Pd-based samples is in line with the higher DeNO<sub>x</sub> performance observed in Fig. 7 under cycled NO<sub>x</sub> storage and reduction periods. The NO<sub>x</sub> reduction assisted by the noble metal allows a deeper regeneration of the NO<sub>x</sub> trapping sites, which eventually results in a higher NO<sub>x</sub> storage and reduction performance. The effect of temperature on the nitrogen containing products yield ( $Y_{\text{N}_2\text{O}}$ ,  $Y_{\text{NH}_3}$  and  $Y_{\text{N}_2}$ ) is also noteworthy (Tables S1–S3). Nitrogen formation is promoted at low temperatures whereas NH<sub>3</sub> at higher temperatures. Thus, in order to drive the selectivity of the NO<sub>x</sub> storage and reduction process towards N<sub>2</sub>, the catalyst must be active at low temperature, which is only possible in the presence of Pd.

During the rich period of the NO<sub>x</sub> storage and reduction experiments shown in Fig. 7, hydrogen reacts with the stored NO<sub>x</sub> generating NH<sub>3</sub>, N<sub>2</sub>O and N<sub>2</sub>. As a general trend, the NH<sub>3</sub> signal is delayed with respect to N<sub>2</sub>O and N<sub>2</sub> signals in all cases. This is due to the proposed regeneration mechanism, which consists of a sequential two-step pathway for nitrogen formation involving the fast formation of NH<sub>3</sub> on

reaction of nitrates with H<sub>2</sub>, followed by the slower reaction of the NH<sub>3</sub> formed with the stored nitrates leading to the selective formation of N<sub>2</sub>. Maximum NH<sub>3</sub> concentration is detected at the reactor outlet for the LSCO/Al<sub>2</sub>O<sub>3</sub> sample. NH<sub>3</sub> formation is lower for Pd-based samples, while nitrogen formation is promoted. Among Pd-based samples, Pd-impregnated sample presented the highest yield of N<sub>2</sub>, probably due to a higher dispersion of the noble metal. This fact facilitates a close contact between the storage sites of the perovskite and the reduction sites and drives the NO<sub>x</sub> reduction towards N<sub>2</sub>.

The NO<sub>x</sub> storage capacity (NSC), global NO conversion ( $X_{\text{NO}}$ ) and nitrogen yield ( $Y_{\text{N}_2}$ ) values for the samples with 0.75, 1.5 and 3.0% of palladium incorporated by doping or impregnation were calculated in the studied temperature range (Fig. 8a.1 and a.2, respectively). NSR model catalyst and Pd-free sample (30% La<sub>0.7</sub>Sr<sub>0.3</sub>CoO<sub>3</sub>/Al<sub>2</sub>O<sub>3</sub>) are also included as reference (Fig. 8a.3). All samples show a volcano-type dependence of the NO<sub>x</sub> storage capacity (NSC) with temperature, typically showing a maximum NSC performance around 350–400 °C. At higher temperatures, NO<sub>x</sub> adsorption capacity tends to decrease due to the lower stability of NO<sub>x</sub> adsorbed species [54,58,59] together with the decreased NO-to-NO<sub>2</sub> conversion (limiting step during the NO<sub>x</sub> storage step), as previously observed in Fig. 6.

Even though Pd does not play a significant role as NO<sub>x</sub> storage component, the higher NSC activity observed for Pd-based samples could be attributed to a deeper regeneration of the NO<sub>x</sub> adsorption sites located on the perovskite (as previously reported for Pt-based samples [60,61]). In agreement with this, the presence of Pd enhanced the hydrogen spillover from Pd to the perovskite sites, which results in a higher availability of NO<sub>x</sub> trapping sites in the subsequent adsorption period [18,26].

Pd-impregnated samples show the best performance with a maximum NSC around 90% at 350–400 °C (Fig. 8a.2), whereas Pd-doped formulations show a maximum of 80% in the same temperature range (Fig. 8a.1). According to the above reported characterization experiments, the higher NSC observed for Pd-impregnated samples could be ascribed to the proximity between Pd and NO<sub>x</sub> adsorption sites, which promotes a faster regeneration of the NO<sub>x</sub> trapping sites.

NO-to-NO<sub>2</sub> conversion is considered as a critical stage for NO<sub>x</sub> adsorption during the NSR process. The higher NO-to-NO<sub>2</sub> conversion for perovskite-based catalysts (Fig. 6) promotes the storage of NO<sub>x</sub> through the nitrate route [9,56,62,63] leading to a higher NSC than with the Pt-based model catalyst (Fig. 8a.3). Above 350 °C, the stability of nitrates formed over the perovskite is lower than the stability of nitrates formed over model NSR catalyst, in good agreement with the results obtained by Li et al. [16].

The incorporation of palladium also improves global NO conversion



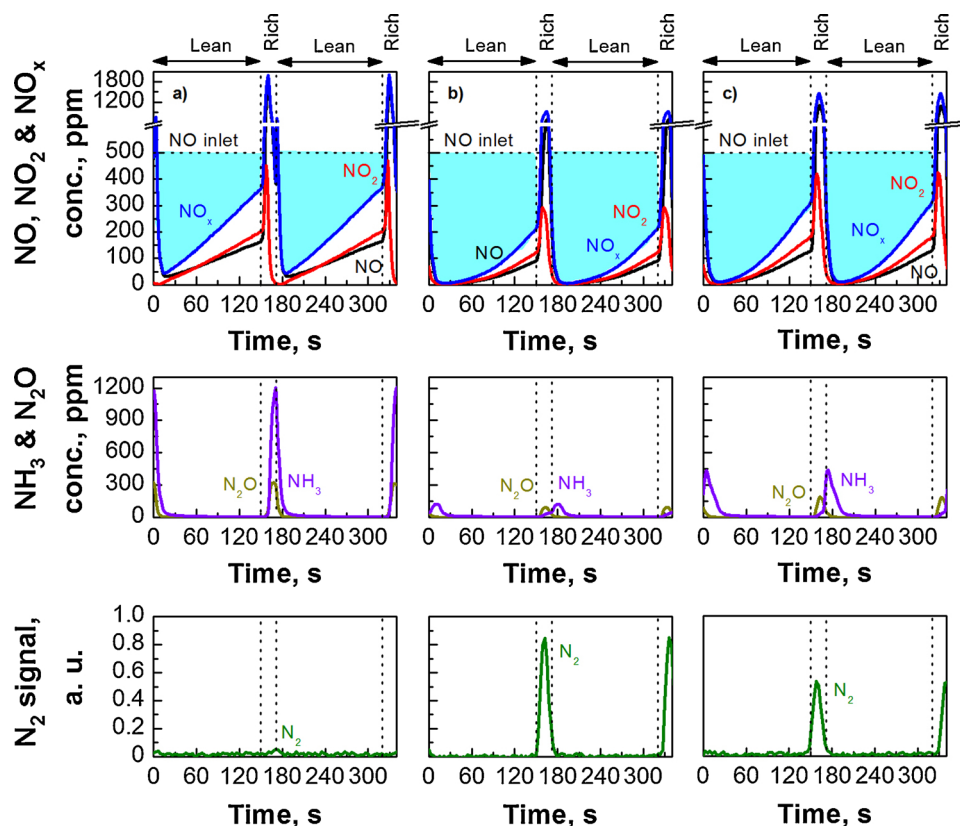


Fig. 7.  $\text{NO}$ ,  $\text{NO}_2$ ,  $\text{NO}_x$  ( $\text{NO} + \text{NO}_2$ ),  $\text{NH}_3$  and  $\text{N}_2\text{O}$  outlet concentration, and MS signal of  $\text{N}_2$  during two consecutive lean-rich cycles in stationary state of: a) 30%  $\text{La}_{0.7}\text{Sr}_{0.3}\text{CoO}_3/\text{Al}_2\text{O}_3$ , and this sample with a 1.5% of palladium incorporated by b) impregnation (1.5% Pd-30%  $\text{La}_{0.7}\text{Sr}_{0.3}\text{CoO}_3/\text{Al}_2\text{O}_3$ ) or c) by doping (30%  $\text{La}_{0.7}\text{Sr}_{0.3}\text{Co}_{0.93}\text{Pd}_{0.11}\text{O}_3/\text{Al}_2\text{O}_3$ ) at 400 °C.

( $X_{\text{NO}}$ ). Pd-impregnated samples with palladium nominal contents above 0.75% show maximum conversion of around 90% at 350–400 °C (Fig. 8b.2), whereas Pd-doped samples maximum conversions are below 80% (Fig. 8b.1). The higher conversion of NO for Pd-impregnated samples could be attributed to the higher amount of  $\text{NO}_x$  stored during lean period [57], as observed in Fig. 8a, and the interaction between Pd and  $\text{NO}_x$  adsorption sites [9], as previously observed by STEM images, XPS and  $\text{H}_2$ -TPR analysis. Pd containing perovskite samples also show higher  $X_{\text{NO}}$  than Pt-based model catalyst at low temperatures (Fig. 8b.3), which is mainly ascribed to their higher  $\text{NO}_x$  storage capacity (Fig. 8a). However, the lower nitrates stability above 400 °C on the Pd-impregnated LSCO/ $\text{Al}_2\text{O}_3$  catalyst (Fig. S4) limits the  $\text{NO}_x$  conversion with respect to the NSR model catalyst at high reaction temperatures.

The evolution of NO-to- $\text{N}_2$  yield (Eq. 7) with temperature is plotted in Fig. 8c. As expected, incorporating palladium significantly improves the nitrogen yield, with  $Y_{\text{N}_2}$  values going from 20% for the LSCO/ $\text{Al}_2\text{O}_3$  sample to a maximum between 40–70% for the Pd-based samples. This is in good agreement with the enhanced  $\text{NO}_x$  storage capacity and  $\text{NO}_x$  reduction. Furthermore, the selectivity towards nitrogen is also promoted with a proportional decrease in ammonia yield (Fig. 8f.1–3). Pd-impregnated samples (Fig. 8c.2) promote significantly the nitrogen yield compared to Pd-doped ones (Fig. 8c.1), which could be again attributed to higher palladium sites accessibility, which are considered as the main active sites for  $\text{NO}_x$ -to- $\text{N}_2$  reduction [26]. In this sense,  $Y_{\text{N}_2}$  increases progressively with palladium content for Pd-doped samples up to 50% at 400 °C for 30%  $\text{La}_{0.7}\text{Sr}_{0.3}\text{Co}_{0.86}\text{Pd}_{0.22}\text{O}_3/\text{Al}_2\text{O}_3$  (LSP(0.22) O/ $\text{Al}_2\text{O}_3$ ) sample. Meanwhile, the maximum nitrogen yield is around 70% at 350 °C for Pd contents above 0.75% for the Pd-impregnated ones. Thus, the impregnation of a 1.5 wt% of palladium is enough to provide appropriate  $\text{NO}_x$  reduction rate to form  $\text{N}_2$ .

The nitrogen yields provided by 1.5% Pd-30%  $\text{La}_{0.7}\text{Sr}_{0.3}\text{CoO}_3/\text{Al}_2\text{O}_3$  sample are similar or even higher than that of the Pt-based model catalyst (Fig. 8c.3). The differences in nitrogen yield are proportional to the  $\text{NO}_x$  storage capacity, suggesting that the  $\text{NO}_x$  adsorption is a key

factor for the subsequent  $\text{NO}_x$ -to- $\text{N}_2$  reduction over these formulations. However, the promotion effect derived from the use of the perovskite phase is partially limited due to the faster nitrates decomposition (Figure S4), leading to a slightly lower nitrogen yield at high temperatures.

To support these results, Fig. 8 also includes the evolution of nitrogen dioxide ( $Y_{\text{NO}_2}$ ), nitrous oxide ( $Y_{\text{N}_2\text{O}}$ ) and ammonia ( $Y_{\text{NH}_3}$ ) yields with reaction temperature. In agreement with the faster regeneration of the  $\text{NO}_x$  adsorption sites, the  $\text{NO}_2$  yield significantly decreases for Pd-based samples with respect to LSCO/ $\text{Al}_2\text{O}_3$  variant (Fig. 8d.1–3). Even though, the  $\text{NO}_2$  yield at 450 °C is almost twice as high as that observed for the NSR model catalysts (Figs. 8d.3) [52], due to the higher oxidation capacity of the perovskite based samples.

As already observed by Qi et al. [57], the maximum  $Y_{\text{NH}_3}$  is observed at high temperatures (400–450 °C) for the LSCO/ $\text{Al}_2\text{O}_3$  sample (Fig. 8f.3), whereas the incorporation of Pd moves the  $\text{NH}_3$  yield to lower temperatures, i.e. 200–300 °C (Fig. 8f.1–2).  $\text{NH}_3$  is produced by the reduction of stored nitrates with  $\text{H}_2$ . The so-formed  $\text{NH}_3$  can react with stored nitrates located downstream or with  $\text{O}_2$  stored over the perovskite, producing  $\text{N}_2$  in both mechanisms [64,65]. Note that the stored oxygen will consume a fraction of the reductant, which can limit the  $\text{NO}_x$  reduction capacity [52]. As a result, the lower  $\text{NH}_3$  yields (< 5%) observed above 250 °C for Pd-based samples (compared with the LSCO/ $\text{Al}_2\text{O}_3$  catalyst) are a consequence of higher  $\text{NO}_x$  adsorption in the form of nitrates, which promotes  $\text{NH}_3$  consumption downstream [66].

However, the decrease in the palladium accessibility observed for Pd-doped samples limits the reduction of stored nitrates and  $\text{N}_2$  yield, and as a consequence, increases the ammonia yield (22–28%) with respect to the Pd-impregnated samples (15–20%). On the other hand, NSR model catalyst shows similar influence of the reaction temperature over ammonia yield (Fig. 8f.3). In agreement with reaction mechanisms previously described, the ammonia yield is lower below 300 °C than that for the Pd-impregnated sample, whereas above this temperature the trend is opposite.

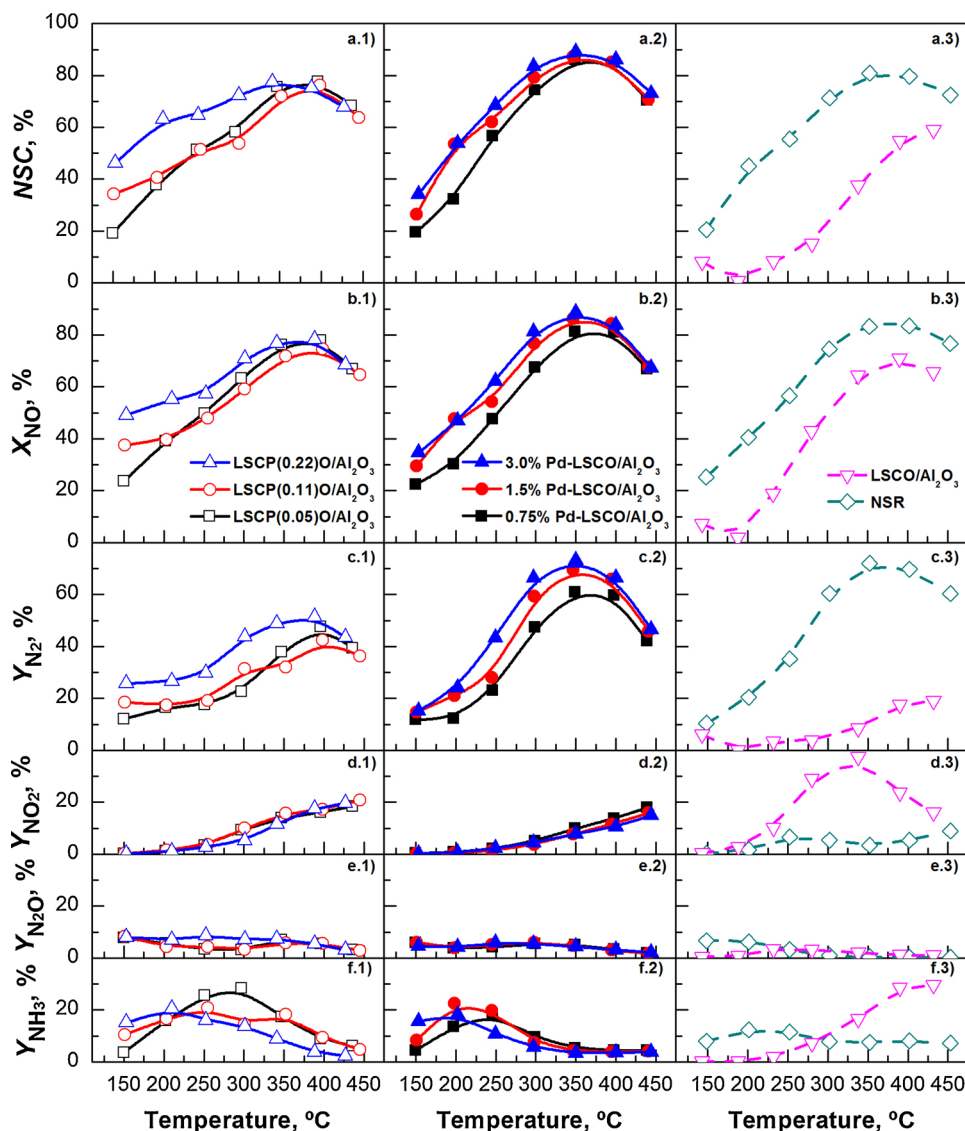


**Fig. 8.** Evolution of: a) NO<sub>x</sub> storage capacity (NSC), b) NO global conversion ( $X_{NO}$ ) and c) nitrogen yield ( $Y_{N_2}$ ) with temperature for alumina-supported perovskite (LSCO/Al<sub>2</sub>O<sub>3</sub>) with a 0.75%, 1.5% and 3.0% of Pd incorporated by impregnation (left column) or by doping (central column). NSR model catalyst (1.5% Pt-15% Ba/Al<sub>2</sub>O<sub>3</sub>) and the sample without Pd are also included as reference (right column).

Finally, in the case of N<sub>2</sub>O yield (Figure 9e.1–3), a slightly promotion can be observed after palladium incorporation. As reported by Li et al. [16], Pd slightly promotes NO dissociation to form N<sub>2</sub>O. In any case, the maximum  $Y_{N_2O}$  is below 8% in all cases, which denotes a low selectivity towards this compound. This suggests that these series of catalysts possess weak capability for the combination of adsorbed NO molecules and N species. Additionally, perovskite-based formulations (Figure 9e.1–2) show slightly higher N<sub>2</sub>O yields than the NSR model catalyst (Figure 9e.3) above 300 °C, but always to a much fewer extent in comparison to other by-products in line with that observed in previous works [67–69]. In this sense, the N<sub>2</sub>O maximum yield is 6.7% and 6.1% at 150 °C for 1.5% Pt-15% BaO/Al<sub>2</sub>O<sub>3</sub> and 1.5% Pd-30% La<sub>0.7</sub>Sr<sub>0.3</sub>CoO<sub>3</sub>/Al<sub>2</sub>O<sub>3</sub> catalysts, respectively.

#### 4. Conclusions

The variation of the preparation method (doping or wetness impregnation), and of the Pd loading result in significant differences with respect to NO<sub>x</sub> removal efficiency of 30% La<sub>0.7</sub>Sr<sub>0.3</sub>CoO<sub>3</sub>/Al<sub>2</sub>O<sub>3</sub> supported perovskites. The doping method only incorporates a part of Pd into the perovskite lattice and then also generates large Pd

nanoparticles on the surface, as evidenced by XRD and Raman analysis, as well as STEM-EDX micrographs. Indeed, the high calcination temperature needed to crystallize the perovskite favours the aggregation of Pd particles resulting in a low dispersion. Meanwhile, the wetness impregnation method leads to homogeneously distributed Pd nanoparticles over alumina-supported perovskite samples surface. As a result, impregnation method leads to an increase of the peak assigned to the reduction of Pd and cobalt in close contact, which confirms that the Pd-perovskite interactions are favoured.

The NO<sub>x</sub> removal efficiency of noble metal-free 30% La<sub>0.7</sub>Sr<sub>0.3</sub>CoO<sub>3</sub>/Al<sub>2</sub>O<sub>3</sub> (LSCO/Al<sub>2</sub>O<sub>3</sub>) sample is significantly promoted by the addition of Pd, especially by using the wetness impregnation method. The NO<sub>x</sub> storage capacity improves from 59% for the reference sample (LSCO/Al<sub>2</sub>O<sub>3</sub>) up to values in the range of 86–89% and 76–80% for Pd-impregnated and Pd-doped samples, respectively. Similarly, the presence of palladium also enhances  $Y_{N_2}$  from 19% for reference sample to values between 42–53% and 61–73% for Pd-doped and Pd-impregnated samples, respectively. This enhancement of the catalytic performances is related to a more efficient regeneration of catalysts surface after the NO<sub>x</sub> adsorption phase due to H<sub>2</sub> spillover from Pd to nearby NO<sub>x</sub> trapping sites in close contact, as well as a faster NO<sub>x</sub> reduction during

rich conditions.

Thus, the best De-NO<sub>x</sub> performance shown by Pd-impregnated samples, especially in terms of NO<sub>x</sub> reduction ability, is due to higher Pd dispersions and synergetic effects with the perovskite phase. This promotes the diffusion of intermediate compounds between NO<sub>x</sub> adsorption and reduction sites. Among the Pd-impregnated samples, 1.5% Pd-30% La<sub>0.7</sub>Sr<sub>0.3</sub>CoO<sub>3</sub>/Al<sub>2</sub>O<sub>3</sub> catalyst presented the best balance between NO<sub>x</sub> removal efficiency and lower noble metal loading. Furthermore, this latter catalyst shows NO-to-NO<sub>2</sub> conversion significantly higher than the Pt-based model catalysts (1.5% Pt-15% BaO/Al<sub>2</sub>O<sub>3</sub>), which results in a significant promotion of NO<sub>x</sub> storage capacity during lean conditions due to the nitrate route promotion. In addition, nitrogen yield is similar or even higher than that achieved with the reference catalyst. Therefore, the developed formulation seems to be promising alternative to the conventional Pt-based catalysts for NO<sub>x</sub> removal in diesel engines using the NO<sub>x</sub> storage and reduction technology.

## Acknowledgments

Support for this study was provided by the Spanish Ministry of Economy and Competitiveness (CTQ2015-67597-C2-1-R) and the Basque Government (IT657-13 and IT1297-19). One of the authors (JAO) was supported by a PhD research fellowship provided by the Basque Government (PRE\_2014\_1\_396). Thanks are due to the CLYM ([www.clym.fr](http://www.clym.fr)) for its guidance in the ETEM project, which was financially supported by the CNRS, the Region Rhône-Alpes, the 'GrandLyon' and the French Ministry of Research and Higher Education.

## Appendix A. Supplementary data

Supplementary material related to this article can be found, in the online version, at doi:<https://doi.org/10.1016/j.apcatb.2019.118052>.

## References

- [1] P. Granger, V.I. Parvulescu, *Chem. Rev.* 111 (2011) 3155–3207.
- [2] B. Pereda-Ayo, R. López-Fonseca, J.R. González-Velasco, *Appl. Catal. A: Gen.* 363 (2009) 73–80.
- [3] B. Pereda-Ayo, U. De La Torre, M. Romero-Sáez, A. Aranzabal, J.A. González-Marcos, J.R. González-Velasco, *Catal. Today* 216 (2013) 82–89.
- [4] D.M. Fernandes, C.F. Scofield, A.A. Neto, M.J.B. Cardoso, F.M.Z. Zotin, *Chem. Eng. J.* 160 (2010) 85–92.
- [5] S. Ponce, M.A. Peña, J.L.G. Fierro, *Appl. Catal. B: Environ.* 24 (2000) 193–205.
- [6] V. Alcalde-Santiago, A. Davó-Quinóner, I. Such-Basáñez, D. Lozano-Castelló, A. Bueno-López, *Appl. Catal. B: Environ.* 220 (2018) 524–532.
- [7] J.A. Onrubia, B. Pereda-Ayo, U. De-La-Torre, J.R. González-Velasco, *Appl. Catal. B: Environ.* 213 (2017) 198–210.
- [8] J.A. Onrubia-Calvo, B. Pereda-Ayo, U. De-La-Torre, J.R. González-Velasco, *Catal. Today* 333 (8WCO) (2018) 208–218.
- [9] X. Wang, X. Qi, Z. Chen, L. Jiang, R. Wang, K. Wei, *J. Phys. Chem. C* 118 (2014) 13743–13751.
- [10] A. Schön, J. Dacquin, P. Granger, C. Dujardin, *Appl. Catal. B: Environ.* 223 (2018) 167–176.
- [11] A. Ueda, Y. Yamada, M. Katsuki, T. Kiyobayashi, Q. Xu, N. Kuriyama, *Catal. Commun.* 11 (2009) 34–37.
- [12] C.H. Kim, G. Qi, K. Dahlberg, W. Li, *Science* 327 (2010) 1624–1627.
- [13] M. Uenishi, M. Taniguchi, H. Tanaka, M. Kimura, Y. Nishihata, J. Mizuki, T. Kobayashi, *Appl. Catal. B: Environ.* 57 (2005) 267–273.
- [14] I. Twagirashema, M. Engelmann-Pirez, M. Frere, L. Burylo, L. Gengembre, C. Dujardin, P. Granger, *Catal. Today* 119 (2007) 100–105.
- [15] Q. Zheng, M. Lail, K. Amato, J.T. Ennis, *Catal. Today* (2017).
- [16] X. Li, C. Chen, C. Liu, H. Xian, L. Guo, J. Lv, Z. Jiang, P. Vernoux, *ACS Catal.* 3 (2013) 1071–1075.
- [17] J.P. Dacquin, C. Dujardin, P. Granger, *J. Catal.* 253 (2008) 37–49.
- [18] Z. Say, M. Dogac, E.I. Vovk, Y.E. Kalay, C.H. Kim, W. Li, E. Ozensoy, *Appl. Catal. B: Environ.* 154–155 (2014) 51–61.
- [19] J. Giraudon, A. Elhachimi, F. Wyrwalski, S. Siffert, A. Aboukaïs, J. Lamoniér, G. Leclercq, *Appl. Catal. B: Environ.* 75 (2007) 157–166.
- [20] R. Zhang, H. Alamdari, S. Kaliaguine, *J. Catal.* 242 (2006) 241–253.
- [21] D.Y. Yoon, Y.J. Kim, J.H. Lim, B.K. Cho, S.B. Hong, I. Nam, J.W. Choung, *J. Catal.* 330 (2015) 71–83.
- [22] C. Li, C. Wang, Y. Lin, *Catal. Today* 174 (2011) 135–140.
- [23] Y. Nishihata, J. Mizuki, T. Akao, H. Tanaka, M. Uenishi, M. Kimura, T. Okamoto, N. Hamada, *Nature* 418 (2002) 164.
- [24] K. Zhou, H. Chen, Q. Tian, Z. Hao, D. Shen, X. Xu, *J. Mol. Catal. A: Chem.* 189 (2002) 225–232.
- [25] G.C.M. Rodríguez, K. Kelm, S. Heikens, W. Grünert, B. Saruhan, *Catal. Today* 184 (2012) 184–191.
- [26] D. Zhao, Z. Gao, H. Xian, L. Xing, Y. Yang, Y. Tian, T. Ding, Z. Jiang, J. Zhang, L. Zheng, X. Li, *Ind. Eng. Chem. Res.* 57 (2018) 521–531.
- [27] J. Zhang, D. Tan, Q. Meng, X. Weng, Z. Wu, *Appl. Catal. B: Environ.* 172–173 (2015) 18–26.
- [28] Y. Wang, X. Cui, Y. Li, Z. Shu, H. Chen, J. Shi, *Microporous Mesoporous Mater.* 176 (2015) 8–15.
- [29] A. Bisht, P. Zhang, C. Shivakumara, S. Sharma, *J. Phys. Chem. C* 119 (2015) 14126–14134.
- [30] X. Guo, M. Meng, F. Dai, Q. Li, Z. Zhang, Z. Jiang, S. Zhang, Y. Huang, *Appl. Catal. B: Environ.* 142–143 (2013) 278–289.
- [31] M. Brun, A. Berthet, J.C. Bertolini, *J. Electron Spectros. Relat. Phenomena* 104 (1999) 55–60.
- [32] S. Cimino, M.P. Casaleto, L. Lisi, G. Russo, *Appl. Catal. A: Gen.* 327 (2007) 238–246.
- [33] Y. Wu, C. Dujardin, C. Lancelot, J.P. Dacquin, V.I. Parvulescu, M. Cabié, C.R. Henry, T. Neisius, P. Granger, *J. Catal.* 328 (2015) 236–247.
- [34] K. Otto, L.P. Haack, J.E. deVries, *Appl. Catal. B: Environ.* 1 (1992) 1–12.
- [35] P. Miquel, Y. Yamin, K. Lombaert, C. Dujardin, M. Trentesaux, L. Gengembre, P. Granger, *Surf. Interface Anal.* 42 (2010) 545–550.
- [36] Y. Lu, A. Eyssler, E.H. Otal, S.K. Matam, O. Brunko, A. Weidenkaff, D. Ferri, *Catal. Today* 208 (2013) 42–47.
- [37] R.J. Farrauto, M.C. Hobson, T. Kennelly, E.M. Waterman, *Appl. Catal. A: Gen.* 81 (1992) 227–237.
- [38] B. Białobok, J. Trawczyński, W. Miśta, M. Zawadzki, *Appl. Catal. B: Environ.* 72 (2007) 395–403.
- [39] W.Y. Jung, Y.I. Song, K.T. Lim, G.D. Lee, M.S. Lee, S.-H. Hong, *J. Nanosci. Nanotechnol.* 15 (2015) 652–655.
- [40] J.A. Villoria, M.C. Alvarez-Galvan, S.M. Al-Zahrani, P. Palmisano, S. Specchia, V. Specchia, J.L.G. Fierro, R.M. Navarro, *Appl. Catal. B: Environ.* 105 (2011) 276–288.
- [41] S. Irusta, M.P. Pina, M. Menéndez, J. Santamaría, *J. Catal.* 179 (1998) 400–412.
- [42] P. Ammendola, E. Cammisa, L. Lisi, G. Ruoppolo, *Ind. Eng. Chem. Res.* 51 (2012) 7475–7481.
- [43] N. Mizuno, H. Fujii, H. Igarashi, M. Misono, *J. Am. Chem. Soc.* 114 (1992) 7151–7158.
- [44] Z. Boukha, J.L. Ayastuy, J.R. González-Velasco, M.A. Gutiérrez-Ortiz, *Appl. Catal. B: Environ.* 201 (2017) 189–201.
- [45] A. Eyssler, A. Winkler, O. Safonova, M. Nachtegaal, S.K. Matam, P. Hug, A. Weidenkaff, D. Ferri, *Chem. Mater.* 24 (2012) 1864–1875.
- [46] S. Sartipi, A.A. Khodadadi, Y. Mortazavi, *Appl. Catal. B: Environ.* 83 (2008) 214–220.
- [47] A. Tou, H. Einaga, Y. Teraoka, *Catal. Today* 201 (2013) 103–108.
- [48] T. Zhang, J. He, W. Xia, H. Hochstadt, J. Yang, Y. Zhao, *Catal. Commun.* 71 (2015) 51–55.
- [49] C. Constantinou, W. Li, G. Qi, W.S. Epling, *Appl. Catal. B: Environ.* 134–135 (2013) 66–74.
- [50] Y. Dong, H. Xian, J. Lv, C. Liu, L. Guo, M. Meng, Y. Tan, N. Tsubaki, X. Li, *Mater. Chem. Phys.* 143 (2014) 578–586.
- [51] A. Ma, S. Wang, C. Liu, H. Xian, Q. Ding, L. Guo, M. Meng, Y. Tan, N. Tsubaki, J. Zhang, L. Zheng, X. Li, *Appl. Catal. B: Environ.* 146 (2014) 24–34.
- [52] G. Qi, W. Li, *Catal. Today* 184 (2012) 72–77.
- [53] S. Hodjati, K. Vaezzadeh, C. Petit, V. Pitchon, A. Kiennemann, *Catal. Today* 59 (2000) 323–334.
- [54] B. Pereda-Ayo, D. Duraiswami, J.J. Delgado, R. López-Fonseca, J.J. Calvino, S. Bernal, J.R. González-Velasco, *Appl. Catal. B: Environ.* 96 (2010) 329–337.
- [55] I. Nova, L. Lietti, L. Castoldi, E. Tronconi, P. Forzatti, *J. Catal.* 239 (2006) 244–254.
- [56] L. Castoldi, L. Righini, R. Matarrese, L. Lietti, P. Forzatti, *J. Catal.* 328 (2015) 270–279.
- [57] B. Pereda-Ayo, U. De La Torre, M.P. González-Marcos, J.R. González-Velasco, *Catal. Today* 241 (Part A) (2015) 133–142.
- [58] X. He, M. Peng, J. He, Z. Zou, X. Li, Z. Li, Z. Jiang, *Catal. Commun.* 12 (2010) 165–168.
- [59] W. Wen, X. Wang, S. Jin, R. Wang, *RSC Adv.* 6 (2016) 74046–74052.
- [60] L. Cumananunge, S.S. Mulla, A. Yezzerets, N.W. Currier, W.N. Delgass, F.H. Ribeiro, *J. Catal.* 246 (2007) 29–34.
- [61] P. Forzatti, L. Lietti, I. Nova, *Energy Environ. Sci.* 1 (2008) 236–247.
- [62] B. Pereda-Ayo, D. Duraiswami, J.A. González-Marcos, J.R. González-Velasco, *Chem. Eng. J.* 169 (2011) 58–67.
- [63] M. AL-Harbi, W.S. Epling, *Appl. Catal. B: Environ.* 89 (2009) 315–325.
- [64] R. You, Y. Zhang, D. Liu, M. Meng, L. Zheng, J. Zhang, T. Hu, *J. Phys. Chem. C* 118 (2014) 25403–25420.
- [65] J. Ye, Y. Yu, M. Meng, Z. Jiang, T. Ding, S. Zhang, Y. Huang, *Catal. Sci. Technol.* 3 (2013) 1915–1918.
- [66] X.-Li, Y.-Dong, H. Xian, W.Y. Hernández, M. Meng, H.-Zou, A.-Ma, T.-Zhang, Z. Jiang, N. Tsubaki, P. Vernoux, *Energy Environ. Sci.* 4 (2011) 3351–3354.